BISTATIC TOMOGRAPHIC GPR IMAGING FOR INCIPIENT PIPELINE LEAKAGE EVALUATION

L. Crocco and F. Soldovieri

National Research Council (CNR)
Institute for the Electromagnetic Sensing of the Environment (IREA)
via Diocleziano 328, I-80124, Napoli, Italy

T. Millington and N. J. Cassidy

School of Physical and Geographical Sciences
Keele University
Keele, Staffordshire, ST5 5BG, U.K.

Abstract—In this work, we present an inverse scattering approach to address the timely detection of damage and leakage from pipelines via multi-bistatic ground penetrating radar (GPR) surveys. The approach belongs to the class of linearized distorted wave models and explicitly accounts for the available knowledge on the investigated scenario in terms of pipe position and size. The inversion is regularized by studying the properties of the relevant linear operator in such a way to guarantee an early warning capability. The approach has been tested by means of synthetic data generated via a finite-difference time-domain forward solver capable of accurately and realistically modeling GPR experiments. The achieved results show that it is possible to detect the presence of leakage even in its first stages of development.

1. INTRODUCTION

Over the past decade, the costs of servicing underground water, sewage and fuel services has raised dramatically, pushing the demand for improved utility location, inspection, characterization and monitoring technologies that are able to give reliable and accurate images of the investigated region [1, 2]. Amongst the other geophysical investigation methods [1, 3–5], ground penetrating radar (GPR) appears to be a promising candidate, as it allows non-invasive, cost-effective, flexible

Corresponding author: L. Crocco (crocco.l@irea.cnr.it).

surveys to be undertaken. In fact, several examples of its application to the detection and monitoring of buried pipelines can be found in the literature [6–12].

With respect to this framework, the increasing interest towards the adoption of microwave tomographic approaches in GPR applications [13–19] is worth to be mentioned. As a matter of fact, as compared to standard GPR processing techniques, microwave tomographic approaches can improve the "data interpretability", by making use of suitable models of the electromagnetic scattering and well-proved tools to achieve stability against the uncertainties on data.

This work deals with the problem of detecting, possibly in its early stage, the leakage from a water pipeline and imaging its temporal evolution. To this aim, a tomographic inversion approach is specifically designed to tackle the problem at hand. The approach takes advantage of the assumed knowledge of the monitored scenario by exploiting in the model the location, size and electric characteristics of the pipeline. This approach has been already applied to a single-fold/multi-receiver GPR configuration [11]; here, we consider the conventional multi-bistatic configuration usually exploited in utility surveys. As the other main topic of the work, we discuss about the choice of the regularization parameter in the inversion. While in [11] the regularization parameter needed in the inversion was determined only by taking into account the expected noise level, here we also constrain it to the features of the scenario. The reconstruction performances of the tomographic algorithm are assessed against synthetic data generated by a finite-difference time-domain (FDTD) forward modeling scheme that is able to simulate realistic GPR experiments [20, 21].

2. A DISTORTED WAVE MODEL FOR THE SCATTERING FROM A LEAKING PIPELINE

Distorted wave models [22] are often adopted in inverse scattering with the aim of reducing the complexity of the problem and improving the reliability and stability of the solution approaches, thanks to the exploitation of a priori information on the scenario under investigation. In the particular case at hand, one can take advantage of the available knowledge on the pipe's position and size to overcome the fact the field backscattered by the pipeline in most cases overwhelms the one scattered by the leakage, unless this latter is large, thus precluding timely detection. Hence, rather than considering the "conventional" homogeneous half-space reference scenario adopted in standard microwave tomographic techniques for GPR applications, one can formulate the inverse scattering problem within the scenario

depicted in Fig. 1, wherein the pipe features are assumed to be known and included in the background scenario, while the leak represents the only "anomaly".

As a further simplification, the targets are assumed to be invariant along the y-axis, which is consistent with the geometry of the modeled environment. Moreover, since one aims at the qualitative and computationally effective characterization of the anomaly, it proves convenient to adopt a linearized scattering model arising from the Born approximation (BA) [22]. Throughout the paper a time factor $\exp(j\omega t)$ is assumed and dropped.

The investigation domain wherein the leakage is assumed to lie is $D = \{[-X_M, X_M] \times [z_{\min}, z_{\min} + \Delta z] - C\}$, C being the circular cross-section of the metallic pipe. All the media are assumed to be non-magnetic (i.e., the magnetic permeability is everywhere that of free space, μ_o), whilst ε_b and σ_b are the soil relative permittivity and conductivity, respectively. By denoting the leak's permittivity and conductivity with ε_{lk} and σ_{lk}, respectively, one can define the frequency dependent *contrast* function χ defined over D as:

$$\chi(\bar{r}, \omega) = \tilde{\varepsilon}_{lk}(\bar{r}, \omega)/\varepsilon_b(\omega) - 1, \tag{1}$$

where $\tilde{\varepsilon}_{lk}(\bar{r}, \omega) = \varepsilon_{lk}(\bar{r}) - j\sigma_{lk}(\bar{r})/\omega\varepsilon_o$ and $\tilde{\varepsilon}_b(\omega) = \varepsilon_b - j\sigma_b/\omega\varepsilon_o$ are the equivalent permittivities of the leak and the soil, respectively, and ε_o is the free space dielectric permittivity.

The incident field source is a time-harmonic filamentary y-directed electric current (TM-polarization) of infinite extent and invariant along the y-axis, whereas the ideal receiving probe is at a fixed offset Δ. The antennae system is moved at N_M locations $x_1, \ldots, x_{N_M}$ along the rectilinear domain $\Gamma = [-X_o, X_o]$ located at the interface $(z = 0)$ and radiates at N_F evenly spaced frequencies in the band W_Ω.
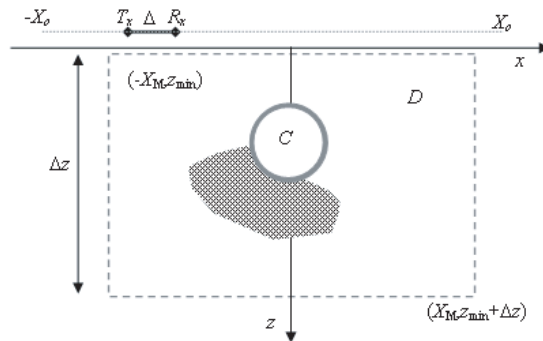

Figure 1. Geometrical parameters and investigated domain. The pipe is assumed to be a part of the background scenario.

In these conditions, the relationship between the contrast and the scattered field, as measured at the generic receiver location $x_m + \Delta$ for the frequency $\hat{\omega}$, is expressed under the BA through the integral equation [22]:

$$E_s(\bar{r}_m, \hat{\omega}) = k_b^2 \int_D G(\bar{r}, \bar{r}_m + \Delta, \hat{\omega}) E_b(\bar{r}, \bar{r}_m, \hat{\omega}) \chi(\bar{r}) d\bar{r}, \qquad (2)$$

where, considering that the inversion only aims at localizing the anomaly, we have assumed that the unknown contrast is frequency independent. In (2), $k_b^2 = \hat{\omega}^2 \tilde{\varepsilon}_b \varepsilon_o \mu_o$ is the wavenumber in the soil, $\bar{r}_m = (x_m, 0)$, $\bar{r} = (x, z)$ and E_b and G denote the background field and the Green's function, respectively, which model the fields when the pipe is intact.

By making the additional simplification of neglecting the presence of the air soil interface, thus considering the scattering phenomenon as occurring in a homogeneous medium with the same properties as the soil, the background field E_b and the Green's function G can be expressed in a closed-form. This is performed in Appendix A by taking advantage of the Fourier-Bessel analytical representations of the fields scattered from a metallic circular cylinder when illuminated by a filamentary current [11, 23].

3. REGULARIZED INVERSION

Given the above relationship between the unknown contrast and the multi-frequency, multi-bistatic scattered field data, the inverse problem is cast into an operator formalism as:

$$E_s = \mathcal{A}_{DB} \mathbf{x}, \qquad (3)$$

where $\mathcal{A}_{DB} : \mathbf{x} \in L^\infty(D) \to E_s \in L^2(\Gamma) \times L^2(W_\Omega)$ is a linear and compact operator whose kernel is given by the product of the Green's function times the background field, see Eq. (2). This kind of linear inverse problem is conveniently solved by exploiting the SVD of $\mathcal{A}_{DB}$, which provides the explicit inversion formula [13, 14, 24]:

$$\mathbf{x} = \sum_{n=0}^{\infty} \frac{1}{\sigma_n} \langle E_s, v_n \rangle u_n. \qquad (4)$$

In (4), σ_n are the singular values, whose magnitude decreases and accumulates to zero for $n \to \infty$, u_n and v_n denotes the left and right singular functions, respectively. In particular, the functions u_n provide a basis for the retrievable functions within the investigated domain D.

As well known, in order to defeat the ill-posedness of the problem, a regularization has to be enforced. This can be accomplished by

truncating the summation (4) at an index $\bar{N}$. By doing so, the resulting Truncated Singular Value Decomposition (TSVD) restricts the solution space to that spanned by the first $\bar{N} + 1$ u_n singular functions [24].

Usually, the choice of $\bar{N}$ is performed as the trade-off between the accuracy of the solution and its stability with respect to uncertainties [13, 14]. These latter may arise from the presence of noise on data and from the limited vallidity of the assumed linear approximation (model mismatch). In the application at hand, the model mismatch is definitely the most important cause of inaccuracy, owing to the presence of significant mutual interactions between the leak and the pipe and to the strong scattering nature of the leak itself, related to the large dielectric permittivity.

To obtain a realible qualitative reconstruction, i.e., stable with respect to model mismatch, one can take advantage of the peculiar features of the considered scenario. In particular, in the case at hand, a satisfying reconstruction is the one that provides information on the presence and the extent of the leakage. Since this latter is located beneath the pipe, it is natural to relate the choice of threshold $\bar{N}$ to this circumstance.

To achieve this purpose, we have carried out an analysis of the "spatial" behaviour of the singular functions u_n. From the observation of these functions, it follows that the deeper parts of the region under test are "imaged" by the large index singular functions. As a consequence, a too small truncation index $\bar{N}$ would lead to a reconstruction that is confined to the shallow part of the investigated domain. Owing to the aforementioned circumstance, it is clear that this would preclude the possibility of detecting and localizing the leakage, especially in its early phases.

For a given scenario, one can achieve a relationship between the truncation index $\bar{N}$ and the spatial domain imaged by the corresponding singular functions' subset, $u_0, \ldots, u_{\bar{N}}$, through the function:

$$\eta(\bar{N}, \bar{r}) = \sum_{n=0}^{\bar{N}} |u_n(\bar{r})|^2 . \qquad (5)$$

As a matter of fact, as shown in Appendix B, this function measures the *energy* of the regularized reconstruction of a point-like scatterer located at $\bar{r}$. As a consequence, the evaluation of the function η for all $\bar{r} \in D$ and for different values of $\bar{N}$, allows one to understand how to fix the threshold by simply observing the function's behavior. In particular, such a choice will result in a trade off between the wish of providing information on the region underneath the pipe and stability of the reconstruction.
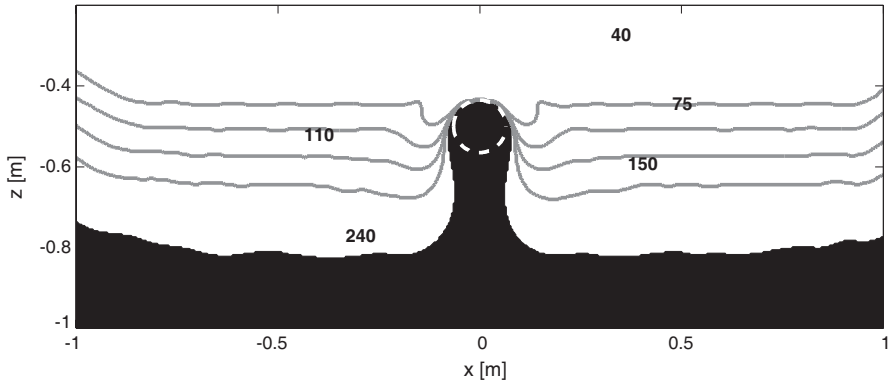
Figure 2. The "quantized" plot of η. The considered threshold indices indicate the area imaged by the corresponding singular functions subset.

Table 1. Parameters of the distorted wave model.

ε_b	σ_b	X_M	$z_{\min}$	Δ_z
3	$0.02\,\mathrm{S/m}$	$1\,\mathrm{m}$	$0.2\,\mathrm{m}$	$0.6\,\mathrm{m}$
N_M	Δ	W_Ω	N_F	
51	$0.18\,\mathrm{m}$	$400\text{--}1300\,\mathrm{MHz}$	19	

The practical tool to perform the choice of $\bar{N}$ is simply given by a plot of $\eta(\bar{N}, \bar{r})$ as "quantized" to a set of threshold indices. For each $\bar{N}$, this plot indicates the subregions of the investigated domain wherein $\eta(\bar{N}, \bar{r})$ is not negligible[†].

As an example, we have illustrated in Fig. 2 the "quantized" energy plot resulting from a typical case, whose specific information corresponds to that of the numerical example given in the next section (and summarized in Table 1). In such a plot, the contour lines delimit the areas in which the function η is meaningful and are labeled with the corresponding value of $\bar{N}$. In contrast, the black solid area represents the "non accessible" region, i.e., the part of the domain which cannot be imaged in a stable way. As can be seen, an incorrect choice of the truncation index (for instance, less than 150) prevents from achieving any information at all on the leak. Conversely, a proper choice of the threshold ($\bar{N} = 240$ in this specific case) allows some information to be extracted from the region behind the pipe, therefore making it possible to detect the presence of the incipient leakage. From the singular values

---

[†] These regions are easily discriminated owing to the abrupt decay of η.

curve depicted in Fig. 3, one can notice that the chosen threshold $\bar{N}$ corresponds to neglect the terms in (4) corresponding to singular values lower than $-30\,\text{dB}$ with respect to the leading one (i.e., σ_0).

4. NUMERICAL EXAMPLES

In this section, the capability of the imaging approach is assessed by applying it to three situations, each describing an incipient (small), advanced (medium) and late (large) leak, respectively (see Fig. 4). The GPR data have been obtained using the 3D FDTD method developed in [20, 21], which incorporates air-soil interface and realistic antenna configurations, accurate source wavelets, truthful material property descriptions to provide reliable numerical simulations of GPR surveys.
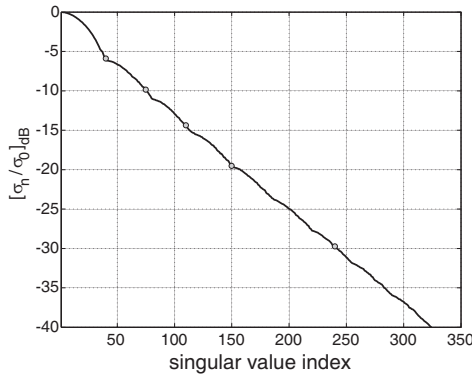

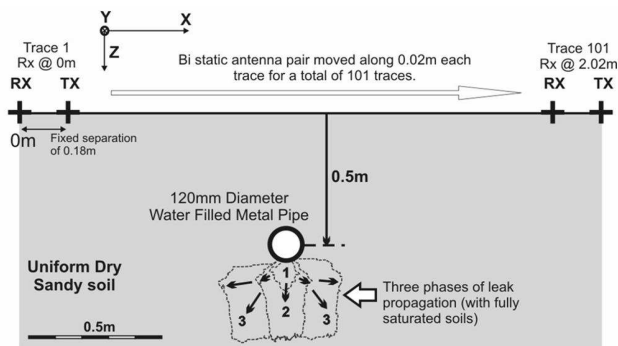**Figure 3.** Singular value spectrum of $\mathcal{A}_{DB}$.

Figure 4. The FDTD model geometry with the form of the spatially expanding water leak.

The simulations consist of a shielded dipole antenna, having a central frequency of 900 MHz, which radiates over a 0.12 m diameter, circular, water-filled metal pipe buried to a depth of 0.5 m in a dry, low-to-medium loss, uniform sandy soil of relative permittivity $\varepsilon_b \approx 3.0$ and a static conductivity of $\sigma_b = 10$ mS/m. The temporally and spatially varying water leakage has been modeled as an incipient, low-flow, low-pressure, gravity-fed leak that emanates from the base of the pipe and soaks the surrounding sands in an expanding saturation front that moves both laterally and vertically downwards across the modeled volume. The saturated soils have frequency-dependent dielectric properties with a relative dielectric permittivity of approximately $\varepsilon_r \approx 22$ at 900 MHz. The synthetic data have been corrupted with an additive Gaussian noise with a signal-to-noise ratio of 20 dB.

The parameters exploited in the distorted wave model are given in Table 1. It is worth to note that in order to apply the inversion algorithm, one has to convert the (synthetic) raw-data radargram (i.e., the total field data in the time-domain) into the desired scattered field data in frequency domain. To achieve this, the total field data is subtracted from the background field in the absence of the leak[‡] and then the resulting time-domain field is Fourier transformed in order to obtain the scattered field data needed by the inversion procedure. According to the discussion in the previous section, the regularized reconstruction **x** is achieved by truncating the SVD to $\bar{N} = 240$. As it can be observed from Fig. 3, where the singular values spectrum has been reported, this corresponds to restricting the summation (4) to the terms weighted by singular values not lower than -30 dB with respect to the leading one (i.e., σ_0).

The results of the inversion algorithm in the three cases are reported in Fig. 5. As can be seen, despite the approximations inherent in the scattering model adopted in the inversion (i.e., ideal probes, 2D geometry, homogeneous background, frequency independent unknown and so on), the approach is able to detect/localize the leak and estimate its extent for both the large and medium leakage examples, (Fig. 5(a) and Fig. 5(b)). By observing Figs. 5(a) and (b), one can notice that some differences arise, revealing the evolving (actually growing) nature of the leak. In particular, a different position of the reconstructed spot is observed. In both cases, the reconstructed spots account for the location of the upper part of the leaks. This latter circumstance is consistent with the fact that the leak almost behaves as a non-penetrable target. Accordingly, only the upper part (directly illuminated by the probing wave) can be imaged. Remarkably,

---

[‡] This latter can be either measured at a different time or spatial location along the pipe or computed by means of the forward solver itself.
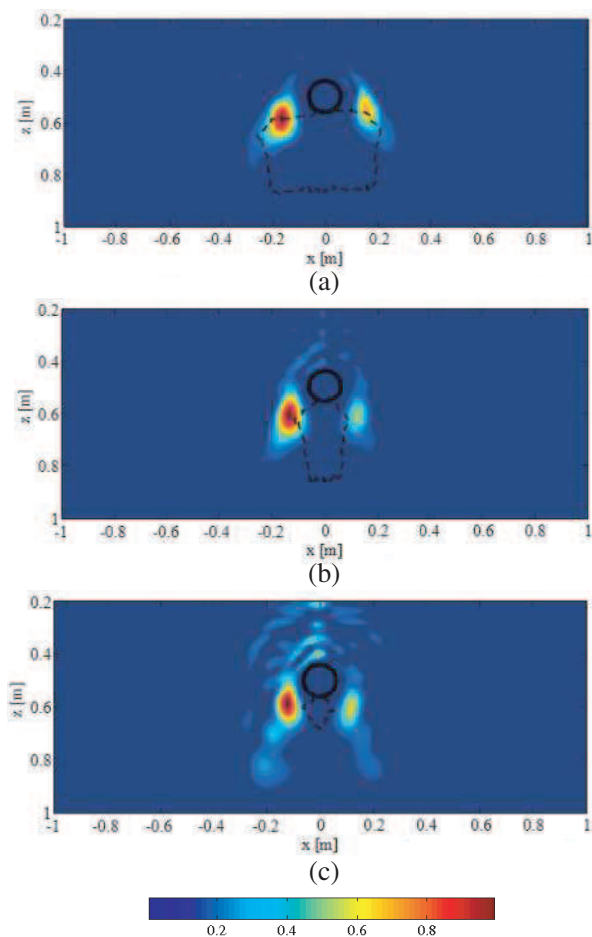
Figure 5. Normalized modulus of the reconstructed contrast achieved through the distorted wave tomographic approach in the three cases of a (a) large; (b) medium, and (c) small leak. In all cases, $\bar{N} = 240$.

as shown in Fig. 5(c), even in the small leak case, where the leak is almost completely masked by the pipe, the presence of an anomaly is clearly detected, thus illustrating the early-time warning capability of the method and its ability to track the evolving leak from its inception. It is worth to note that the features of the reconstruction obtained in the small leak case are consistent with the properties of the spatial function η shown in Fig. 2 and can be explained according to them. As a matter of fact, the region where the leak lies belongs to the non-accessible zone in Fig. 2. Accordingly, a correct localization of the leakage at this stage is not possible. Nevertheless, the algorithm can

help to reveal the presence of the leakage by providing a reconstructed contrast whose modulus is remarkably different from zero in that part of the "accessible" zone which is closer to the leakage. It is also worth to note that the features of such a reconstruction are indeed different from those achieved in the case when there is no leak at all. These results are not shown for the sake of brevity, but the reader is addressed to [11] to appraise the features of the reconstruction when no leak is present, as well as the stability of the proposed inversion method against an incorrect assumption on the pipe's position.
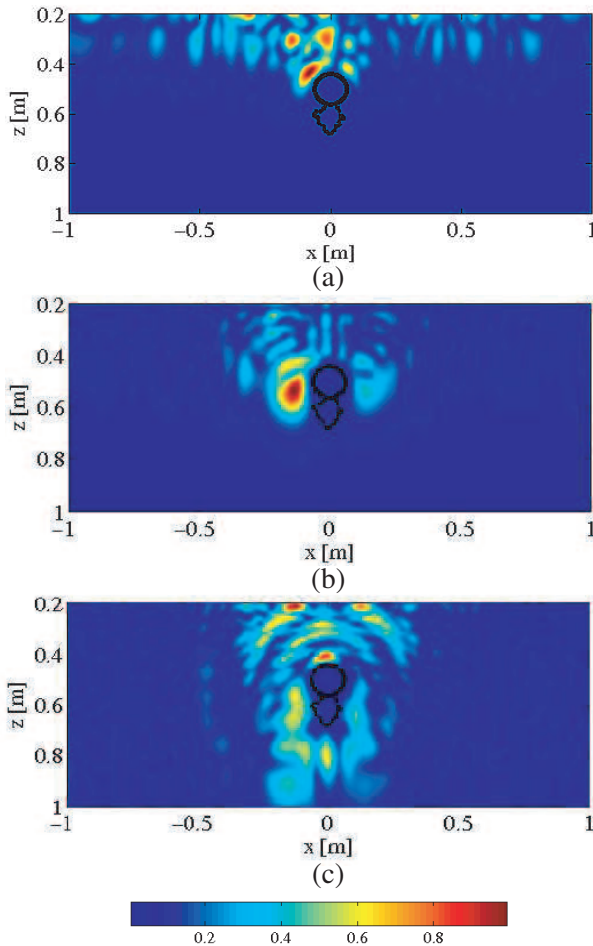

Figure 6. The effect of SVD truncation on the reconstruction achieved in the small leak case. (a) $\bar{N} = 75$; (b) $\bar{N} = 150$; (c) $\bar{N} = 325$.

To point out the effect of SVD truncation index on the trade-off between the stability of the solution and the capability of imaging beneath the pipe, in Fig. 6 we have reported the reconstructions achieved in the small leak case for three different values of $\bar{N}$. First, let us observe Fig. 6(a) which shows the result achieved when a too low number of terms ($\bar{N} = 75$, corresponding to $20 \log 10(\sigma_0/\sigma_{\bar{N}}) = 10\,\text{dB}$ in Fig. 3) is considered. In this case, one can notice how, the inversion algorithm is not able to image the deeper part of the investigation domain where the leak is actually located, as predicted from Fig. 2). In particular, the reconstructed contrast is erroneously localized in the shallower zone and no reliable information can be achieved on the presence and actual position of the leak. Fig. 6(b) shows how the reconstruction slightly improves when taking $\bar{N} = 150$ (that corresponds to a $20\,\text{dB}$ threshold in Fig. 3). As can be seen, the reconstructed contrast is now located in a deeper zone, as compared to the previous case, but yet the leak is not properly localized. Finally, the result corresponding to $\bar{N} = 325$ ($40\,\text{dB}$) is reported in Fig. 6(c). This last case gives a clear example of the instabilities resulting from retaining a number of singular values larger the optimal one in the TSVD expansion. As a matter of fact, the amplification of errors (both model errors and noise on data) entails that the information about the leak location is completely overwhelmed by artifacts.

5. CONCLUSION

In this paper, we have presented a microwave tomographic approach specifically designed for the detection, localization and imaging of an incipient water leak from a metallic buried pipe from bistatic GPR data. To this aim, the underlying inverse scattering problem has been cast within a distorted wave model in which the pipe position and size are accounted for and the leak is the only anomaly. The resulting linear inverse problem is then solved via TSVD and the threshold index is properly fixed by inspecting the properties of the singular functions that span the unknowns' space. This analysis is necessary in order to allow the inversion algorithm to achieve the positive results obtained against synthetic data simulated under realistic conditions. Let us remark that similar results would not be possible by using standard GPR processing or microwave tomographic approaches based on a non-distorted model. Both theoretical and experimental developments will be considered in the continuation of this research activity. As far as the first are concerned, we will aim at determining the minimum size of a detectable leak by the inversion approach as well as the effect of the inaccuracies in the knowledge of the background medium. In addition,

an experimental validation is also in order, possibly carried out with similar methodologies as those considered in [12].

ACKNOWLEDGMENT

APPENDIX A.

Under the assumption that the scattering phenomenon occurs in a homogeneous medium with the same properties of the soil, the background field E_b and the Green's function G are given by the closed-form expressions arising from the Fourier-Bessel analytical representations of the fields scattered from a metallic circular cylinder under the incidence of the field radiated by a filamentary current [23].

In particular, the background field is given by:

$$E_b(\bar{r}, \bar{r}_m, \hat{\omega})$$
$$= -\frac{\hat{\omega}\mu_o}{4}\left[H_0^{(2)}(k_b|\bar{r}-\bar{r}_m|) - \sum_{n=-\infty}^{\infty}\frac{J_n(k_bR)}{H_n^{(2)}(k_bR)}e^{jn[\angle(\bar{r}-\bar{r}_c)-\angle(\bar{r}_m-\bar{r}_c)]}\right.$$
$$\left.\times H_n^{(2)}(k_b|\bar{r}-\bar{r}_c|)H_n^{(2)}(k_b|\bar{r}_m-\bar{r}_c|)\right], \tag{A1}$$

while the Green's function:

$$G(\bar{r}, \bar{r}_m + \Delta, \hat{\omega})$$
$$= -\frac{j}{4}\left[H_0^{(2)}(k_b|\bar{r}_m+\Delta-\bar{r}|) - \sum_{n=-\infty}^{\infty}\frac{J_n(k_bR)}{H_n^{(2)}(k_bR)}e^{jn[\angle(\bar{r}_m+\Delta-\bar{r}_c)-\angle(\bar{r}-\bar{r}_c)]}\right.$$
$$\left.\times H_n^{(2)}(k_b|\bar{r}_m + \Delta - \bar{r}_c|)H_n^{(2)}(k_b|\bar{r} - \bar{r}_c|)\right]. \tag{A2}$$

In Eqs. (A1), (A2), R is the pipe radius, $\bar{r}_c$ its center, J_n the Bessel function of first kind, $H_n^{(2)}$ the Hankel function of second kind and n-th order and $\angle$ the angle between two vectors.

APPENDIX B.

In order to provide an interpretation of the function $\eta(\bar{N}, \bar{r})$ introduced in (5), let us first consider the regularized reconstruction of a contrast

function given by a Dirac pulse located at $\bar{r}'$. From the SVD properties [24] and from (2) and (4), this latter is given by:

$$\mathcal{R}_\delta(\bar{r}; \bar{r}') = \sum_{n=0}^{\bar{N}} u_n^*(\bar{r}') u_n(\bar{r}). \tag{B1}$$

Then, let us evaluate the energy $\mathcal{E}$ of $\mathcal{R}_\delta(\bar{r}; \bar{r}')$, meant as a function of the spatial variable $\bar{r}'$. This latter is given by:

$$\begin{aligned}
\mathcal{E} &= \int_D \sum_{n=0}^{N} u_n^*(\bar{r}') u_n(\bar{r}) \sum_{m=0}^{N} u_m(\bar{r}') u_m^*(\bar{r}) d\bar{r} \\
&= \sum_{n=0}^{N} \sum_{m=0}^{N} u_n^*(\bar{r}') u_m(\bar{r}') \int_D u_n(\bar{r}) u_m^*(\bar{r}) d\bar{r} \\
&= \sum_{n=0}^{N} \sum_{m=0}^{N} u_n^*(\bar{r}') u_m(\bar{r}') \delta(n-m) = \sum_{n=0}^{N} \left| u_n(\bar{r}') \right|^2 \tag{B2}
\end{aligned}$$

where we have exploited the orthonormality of the singular functions in D.

By comparing (B2) and (5), it follows that, for a given location $\bar{r}' \in D$ and a given regularization index $\bar{N}$, the function η corresponds to the energy of the regularized reconstruction of a point-like scatterer located $\bar{r}'$. Therefore, if η attains a low level in a generic point $\bar{r}'$, this indicates that it is not possible to achieve a meaningful reconstruction in that location. Accordingly, the plot of the function η gives an indication of the regions that, for a fixed truncation index, cannot be imaged by a regularized inversion scheme.

REFERENCES

1. Desilva, D., S. Burn, G. Tjandraatmadja, M. Moglia, P. Davis, L. Wolf, I. Held, J. Vollertsen, W. Williams, and L. Hafskjold, "Sustainable management of leakage from wastewater pipelines," *Water Science and Technology*, Vol. 52, No. 12, 189–198, 2005.

2. Upson, S., "How to see the unseen city," *IEEE Spectrum*, Vol. 44, No. 6, 36–37, Jun. 2007.

3. Soleimani, M., C. N. Mitchell, R. Banasiak, R. Wajman, and A. Adler, "Four-dimensional electrical capacitance tomography imaging using experimental data," *Progress In Electromagnetics Research*, PIER 90, 171–186, 2009.

4. Goharian, M., M. Soleimani, and G. R. Moran, "A trust region subproblem for 3D electrical impedance tomography inverse

problem using experimental data," *Progress In Electromagnetics Research*, PIER 94, 19–32, 2009.

5. Banasiak, R., R. Wajman, D. Sankowski, and M. Soleimani, "Three-dimensional nonlinear inverstion of electrical capacitance tomography data using a complete sensor model," *Progress In Electromagnetics Research*, PIER 100, 219–234, 2010.

6. Gamba, P. and S. Lossani, "Neural detection of pipe signatures in ground penetrating radar images," *IEEE Trans. Geosci. Remote Sens.*, Vol. 38, No. 2, 790–797, Mar. 2000.

7. Stampolidis, A., P. Soupios, F. Vallianatos, and G. N. Tsokas, "Detection of leaks in buried plastic water distribution pipes in urban places — A case study," *Proceedings of the 2nd International Workshop on Advanced Ground Penetrating Radar, IWAGPR2003*, 120–124, Delft, The Netherlands, May 2003.

8. Nakhkash, M. and M. R. Mahmood-Zadeh, "Water leak detection using ground penetrating radar," *Proceedings of the 10th International Conference on Ground Penetrating Radar, GPR2004*, 525–528, Delft, The Netherlands, Jun. 2004.

9. Borgioli, G., L. Capineri, P. L. Falorni, S. Matucci, and C. G. Windsor, "The detection of buried pipes from time-of-flight radar data," *IEEE Trans. Geosci. Remote Sens.*, Vol. 46, No. 8, 2254–2266, Aug. 2008.

10. Soldovieri, F., A. Brancaccio, G. Prisco, G. Leone, and R. Pierri, "A Kirchhoff based shape reconstruction algorithm for the multimonostatic configuration: The realistic case of buried pipes," *IEEE Trans. Geosci. Remote Sens.*, Vol. 46, No. 10, 3031–3038, Oct. 2008.

11. Crocco, L., G. Prisco, F. Soldovieri, and N. J. Cassidy, "Earlystage leaking pipes GPR monitoring via microwave tomographic inversion," *Journal of Applied Geophysics*, Vol. 67, No. 4, 270–277, April 2009.

12. Pettinelli, E., F. Soldovieri, A. Di Matteo, L. Crocco, E. Mattei, D. Redman, and P. Annan, "GPR response from buried pipes: measurement on field site and tomographic reconstructions," *IEEE Trans. Geosci. Remote Sens.*, Vol. 8, 2639–2645, Aug. 2009.

13. Soldovieri, F., J. Hugenschmidt, R. Persico, and G. Leone, "A linear inverse scattering algorithm for realistic GPR applications," *Near Surface Geophysics*, Vol. 5, No. 1, 29–41, Feb. 2007.

14. Catapano, I., L. Crocco, R. Persico, M. Pieraccini, and F. Soldovieri, "Linear and nonlinear microwave tomography approaches for subsurface prospecting: Validation on real data," *IEEE Antennas and Wireless Propagation Letters*, Vol. 5, No. 1,

49–53, Dec. 2006.

15. Bermani, E., S. Caorsi, and M. Raffetto, "An inverse scattering approach based on a neural network technique for the detection of dielectric cylinders buried in a lossy half-space," *Progress In Electromagnetics Research*, PIER 26, 67–87, 2000.

16. Cui, T. J., W. C. Chew, X. X. Yin, and W. Hong, "Study of resolution and super resolution in electromagnetic imaging for half-space problems," *IEEE Trans. Antennas and Propagation*, Vol. 52, No. 6, 1398–1411, 2004.

17. Yu, Y., T. Yu, and L. Carin, "Three-dimensional inverse scattering of a dielectric target embedded in a lossy half-space," *IEEE Trans. Geosci. Remote Sens.*, Vol. 42, No. 5, 957–973, 2004.

18. Chommeloux, L., C. Pichot, and J. C. Bolomey, "Electromagnetic modeling for microwave imaging of cylindrical buried inhomogeneities," *IEEE Trans. Microwave Theory Tech.*, Vol. 34, No. 10, 1064–1076, 1986.

19. Meincke, P., "Linear gpr inversion for lossy soil and a planar air-soil interface," *IEEE Trans. Geosci. Remote Sens.*, Vol. 39, No. 12, 2713–2721, 2001.

20. Millington, T. M. and N. J. Cassidy, "Optimising GPR modelling: A practical, multi-threaded approach to 3D FDTD numerical modeling," *Proceedings of the 12th International Conference on Ground Penetrating Radar, GPR2008*, page on CD, Birmingham, UK, Jun. 2008.

21. Cassidy, N. J., "A review of practical numerical modeling methods for the advanced interpretation of ground-penetrating radar in near-surface environments," *Near Surface Geophysics*, Vol. 5, No. 1, 5–22, 2007.

22. Chew, W. C., *Waves and Fields in Inhomogeneous Media*, Institute of Electrical and Electronics Engineers, Piscataway, NJ, 1995.

23. Balanis, C. A., *Advanced Engineering Electromagnetic*, John Wiley, New York, NY, 1989.

24. Bertero, M. and P. Boccacci, *Introduction to Inverse Problems in Imaging*, Institute of Physics Publishing, Bristol and Philadelphia, 1998.